J. Fluid Mech. (2024), *vol*. 1000, A58, doi:10.1017/jfm.2024.996

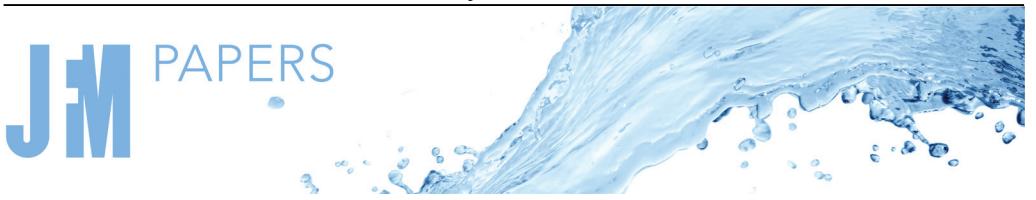

How wide must Rayleigh–Bénard cells be to prevent finite aspect ratio effects in turbulent flow?

Richard J.A.M. Stevens[1,†], **Robert Hartmann**[1], **Roberto Verzicco**[1,2,3] **and Detlef Lohse**[1,4,†]

[1]Physics of Fluids Group, Max Planck Center for Complex Fluid Dynamics and J. M. Burgers Center for Fluid Dynamics, Department of Science and Technology, University of Twente, 7500 AE Enschede, The Netherlands

[2]Dipartimento di Ingegneria Industriale, University of Rome 'Tor Vergata', 00133 Rome, Italy

[3]Gran Sasso Science Institute, 67100 L'Aquila, Italy

[4]Max Planck Institute for Dynamics and Self-Organization, 37077 Göttingen, Germany

(Received 26 February 2024; revised 25 July 2024; accepted 8 October 2024)

We employ direct numerical simulations to investigate the heat transfer and flow structures in turbulent Rayleigh–Bénard convection in both cylindrical cells and laterally periodic domains, spanning an unprecedentedly wide range of aspect ratios $0.075 \leqslant \Gamma \leqslant 32$. We focus on Prandtl number $Pr = 1$ and Rayleigh numbers $Ra = 2 \times 10^7$ and $Ra = 10^8$. In both cases, with increasing aspect ratio, the heat transfer first increases, then reaches a maximum (which is more pronounced for the cylindrical case due to confinement effects), and then slightly goes down again before it finally saturates at the large aspect ratio limit, which is achieved already at $\Gamma \approx 4$. Already for $\Gamma \gtrsim 0.75$, the heat transfers in both cylindrical and laterally periodic domains become identical. The large-Γ limit for the volume-integrated Reynolds number and the boundary layer thicknesses are also reached at $\Gamma \approx 4$. However, while the integral flow properties converge at $\Gamma \approx 4$, the confinement of a cylindrical domain impacts the temperature and velocity variance distributions up to $\Gamma \approx 16$, as thermal superstructures cannot form close to the sidewall.

Key words: Bénard convection, turbulent convection, turbulence simulation

1. Introduction

Rayleigh–Bénard convection (RBC) is the most widely studied model of thermal convection (Ahlers, Grossmann & Lohse 2009; Lohse & Xia 2010; Chilla & Schumacher

† Email addresses for correspondence: r.j.a.m.stevens@utwente.nl, d.lohse@utwente.nl

2012; Xia 2013; Shishkina 2021; Lohse & Shishkina 2023; Xia *et al.* 2023). This model's dimensionless control parameters are the Rayleigh number Ra and the Prandtl number Pr, which respectively characterize the dimensionless temperature difference and fluid properties, and the aspect ratio Γ, which is defined as the system's width over height. The unifying theory of thermal convection has significantly advanced the theoretical understanding of the flow's global transfer properties (Grossmann & Lohse 2000, 2001, 2002, 2004; Ahlers *et al.* 2009; Stevens *et al.* 2013). This Grossmann–Lohse (GL) theory accurately predicts the relationship between the Nusselt number Nu (the non-dimensionalized heat transport) and the Reynolds number Re (the non-dimensionalized flow strength) as a function of Ra and Pr.

Observations at moderate Ra values have demonstrated that appropriate lateral confinement can significantly enhance heat transport, due to the enhancement of vertically coherent flow structures (Huang *et al.* 2013; Chong *et al.* 2015, 2017; Zhang & Xia 2023; Ren *et al.* 2024). Moreover, Hartmann *et al.* (2021) showed that the extent of heat transfer enhancement due to confinement depends strongly on the system's geometry, with a greater enhancement observed in cylindrical cells compared to rectangular or square ones.

Both the onset of convection and the transition to the ultimate regime occur at significantly higher Ra in very small aspect ratio cells. Theoretical and numerical studies have quantified the increase in the critical Rayleigh number Ra_c for the onset of convection (see e.g. Charlson & Sani 1970) and the typical Rayleigh numbers Ra^* for the transition to the ultimate regime, namely as $Ra_c \propto \Gamma^{-4}$ for the onset of convection (Shishkina 2021; Ahlers *et al.* 2022; Zhang & Xia 2023; Ren *et al.* 2024) and as $Ra^* \propto \Gamma^{-3}$ for the onset of the ultimate regime (Roche *et al.* 2010; Roche 2020; Ahlers *et al.* 2022). The existence of an ultimate regime with enhanced heat transport properties and turbulent boundary layers (BLs) had initially been predicted by Kraichnan (1962) and later by Spiegel (1972) and by Grossmann & Lohse (2000, 2001, 2011). The transition to the ultimate regime has meanwhile been observed in various experiments (Chavanne *et al.* 1997; Roche *et al.* 2010; He *et al.* 2012) and has been interpreted to be of non-normal nonlinear type (Roche 2020; Lohse & Shishkina 2023). The simulations presented in this present work do not reach the ultimate regime, which therefore is not discussed further in the main part of this paper, and is readdressed only in the final outlook part of the conclusions.

In nature, convection frequently occurs in very large to infinite domains, facilitating the formation of large-scale turbulent superstructures. For RBC just above the onset, numerous experiments (Fitzjarrald 1976; Bodenschatz, Pesch & Ahlers 2000; Sun *et al.* 2005; du Puits, Resagk & Thess 2007; Xia, Sun & Cheung 2008; Zhou *et al.* 2012; Hogg & Ahlers 2013; du Puits, Resagk & Thess 2013) and simulations conducted in large periodic domains (Hartlep, Tilgner & Busse 2003; Parodi *et al.* 2004; Hartlep, Tilgner & Busse 2005; von Hardenberg *et al.* 2008) as well as in very large aspect ratio cylindrical domains (Shishkina & Wagner 2005, 2006; Bailon-Cuba, Emran & Schumacher 2010; Emran & Schumacher 2015; Sakievich, Peet & Adrian 2016) have unveiled remarkable flow patterns. Correlations between single-point measurements (du Puits *et al.* 2007, 2013) and particle image velocimetry measurements (Xia *et al.* 2008) have indicated a transition from a single-roll to a multi-roll structure as Γ exceeds approximately 4.

Recent simulations by Stevens *et al.* (2018) have revealed that turbulent superstructures persist up to $Ra = 10^9$, with the size of these superstructures increasing with Ra, at least up to $Ra = 10^9$. Visualizations by Pandey, Scheel & Schumacher (2018) and Stevens *et al.* (2018) suggest that large-scale structures are more pronounced in the temperature field than in the velocity field. However, a scale-by-scale analysis using the linear coherence spectrum to examine the correlation between the two fields reveals a near-perfect

correlation at the superstructure scale (Krug, Lohse & Stevens 2020). Furthermore, it has been demonstrated that approximately 30 % of the heat transfer can be attributed to these large-scale flow structures. As the organization of the large-scale flow varies with Γ, the heat transport in the large aspect ratio limit ($\Gamma \gtrsim 4$) is found to be approximately 10 % lower for $Ra = 2 \times 10^7$ and approximately 4 % lower for $Ra = 10^9$ compared to $\Gamma = 1$ (Stevens *et al.* 2018).

Despite these efforts, the flow characteristics in large aspect ratio RBC remain insufficiently documented and understood. Notably, direct one-to-one comparisons between laterally periodic and confined domain simulations have not been performed. Previous simulations for large Γ in cylindrical cells (Bailon-Cuba *et al.* 2010) failed (for the reason, refer to the Appendix) to identify a large-Γ limit, which in contrast was observed in periodic domains (Stevens *et al.* 2018). To bridge this gap in the literature, in this paper we perform direct numerical simulations (DNS) in unprecedentedly large cylindrical domains, $0.075 \leqslant \Gamma \leqslant 32$, achieving up to $Ra = 10^8$. This allows for direct comparisons between cylindrical domains and laterally periodic domains in the limit of very large aspect ratios, showing that the main flow characteristics within these domains become identical as the aspect ratio increases.

The remainder of the paper is organized as follows. Section 2 provides details of the simulation dataset. Section 3 discusses the evolution of Nu and integral Re as a function of Γ. Subsequently, in § 4, we analyse the effects of the system geometry and Γ on the flow structures and velocity and temperature variance distributions in the domain. The paper ends with a summary, conclusions, and an outlook (§ 5).

2. Simulations

We perform DNS of RBC in large cylindrical domains with aspect ratios $0.075 \leqslant \Gamma \leq 32$, solving the incompressible Navier–Stokes equations and the heat transfer equation in Oberbeck–Boussinesq approximation (Ahlers *et al.* 2009). The simulations employ a second-order, energy-conserving finite difference method. This method was initially developed by Verzicco & Orlandi (1996) and Verzicco & Camussi (1997), and has been validated extensively against experiments (Stevens, Verzicco & Lohse 2010*b*; Stevens, Lohse & Verzicco 2011; Stevens *et al.* 2013). Its latest optimized version used here is validated against spectral element methods and fourth-order finite volume schemes (Kooij *et al.* 2018).

The control parameters are defined as $Ra = \alpha g \Delta L^3/(\nu\kappa)$ and $Pr = \nu/\kappa$, where α represents the thermal expansion coefficient, g is the gravitational acceleration, Δ denotes the temperature difference between the top and bottom plates, L is the height of the fluid domain, ν is the kinematic viscosity, and κ is the thermal diffusivity of the fluid. In total, 20 simulations were conducted for $Ra = 2 \times 10^7$ and 10^8, while Pr is fixed at 1. The bottom and top plates were assigned no-slip, constant-temperature boundary conditions, while the sidewall was treated as no-slip and adiabatic.

All simulations were executed carefully to ensure consistency, following the resolution criteria established in previous works (Shishkina *et al.* 2010; Stevens *et al.* 2010*b*). In this context, we also refer to the supplementary material of Ahlers *et al.* (2022), which in its § III explicitly states the requirements on the quality of DNS of turbulent thermal convection, with respect to both spatial resolution and time averaging. To give an example on the resolution, the $Ra = 10^8$ and $\Gamma = 32$ simulation was conducted on an $18\,432 \times 3072 \times 192$ grid. The statistical convergence of integral flow quantities, such as Nu and Re, was within a fraction of 1 %. Achieving such excellent convergence is highly challenging

and relies on meticulous simulation design. Due to the slow dynamics of the thermal superstructures, the convergence of higher-order statistics is inevitably less good than for the integral flow characteristics. The simulations were performed for very long durations, specifically for $\Gamma > 1$, ≈750 dimensionless time units (measured as all times in terms of L/U_{ff}, where $U_{ff} = \sqrt{\alpha g \Delta L}$ is the free-fall velocity) for $Ra = 2 \times 10^7$, and ≈500 time units at $Ra = 10^8$. For $\Gamma \lesssim 1$, 1000 to 10 000 dimensionless time units were considered. The first 100 time units were disregarded as transients. These simulation times exceed the typical duration considered in RBC simulations. Despite the simulations being conducted for extended periods, the recorded flow dynamics in the form of movies indicates that the time required for thermal superstructures to alter their position within the vast domains exceeds the duration of our simulations.

3. Integral heat transport and flow strength

For Rayleigh–Bénard flow in the cylindrical cell, and very small aspect ratio Γ (very slender cells), the Nusselt number is 1, i.e. pure diffusive transport, due to the stabilization by the sidewalls. The critical aspect ratio Γ_c beyond convection sets in depends on Ra as $\Gamma_c \propto Ra^{-1/4}$ (Shishkina 2021; Ahlers *et al.* 2022; Zhang & Xia 2023; Ren *et al.* 2024). When further increasing Γ, one obtains a maximum in $Nu/Ra^{1/3}$, as can be seen from figure 1(*a*). The maximal heat transport is due to the stabilization of the large-scale convection (LSC) due to intermediate confinement. This effect has been observed previously in rectangular cells (Huang *et al.* 2013; Chong *et al.* 2015, 2017), and more recently in square and cylindrical domains (Hartmann *et al.* 2021, 2022; Zhang & Xia 2023; Ren *et al.* 2024). Beyond the maximum, with again further increasing aspect ratio, $Nu/Ra^{1/3}$ decreases again, before reaching a plateau value beyond $\Gamma \gtrsim 4$. We performed well-resolved numerical simulations with aspect ratios as large as $\Gamma = 32$. We note that beyond $\Gamma \gtrsim 4$ (or even not beyond the position of the maximum at $\Gamma \approx 0.3$ or even less for higher Ra), there is no increase of the heat transport with increasing Γ, as was erroneously stated in Bailon-Cuba *et al.* (2010). In that publication, the increase of the heat transfer with increasing Γ is due to increasingly insufficient grid resolution; see the Appendix.

Figure 1(*a*) also compares the heat transport in RBC in the cylindrical domains with that in a periodic domain, both over an unprecedented range of aspect ratios. For small Γ, the heat transport in the periodic domain is smaller than for the cylindrical cell, because in the periodic case, a pronounced vertical temperature gradient is formed in the bulk, weakening the convective flow. However, from $\Gamma \approx 0.75$ onwards, the heat transfers for the periodic domain and for the cylindrical cell agree pretty well.

For $\Gamma \approx 1$, the simulation results agree perfectly with the GL theory, which had been fitted to $\Gamma = 1$ data (Grossmann & Lohse 2000, 2001; Stevens *et al.* 2013). At the same time, at $Ra = 10^8$, the heat transport in the large-Γ limit is approximately 5 % below the $\Gamma = 1$ value. This reduction becomes less with increasing Ra (Stevens *et al.* 2018). The lower heat transport in the large-Γ regime is due to the increased horizontal mixing in horizontally extended systems. For $\Gamma \gtrsim 1$, the heat transports in periodic and cylindrical domains agree exceptionally well, and the large-Γ limit for the heat transport is reached for $\Gamma \gtrsim 4$. Therefore, although heat transport can be influenced by the arrangement of large-scale flow structures (as indicated by the Γ dependence), it does not appear to depend on the system's geometry for sufficiently wide domains. This observation is supported by figure 2, demonstrating the formation of comparable flow structures in periodic and cylindrical domains for $\Gamma = 32$. For this very large aspect ratio $\Gamma = 32$ and for the case of the cylindrical cell, we also show a snapshot of the temperature field in its

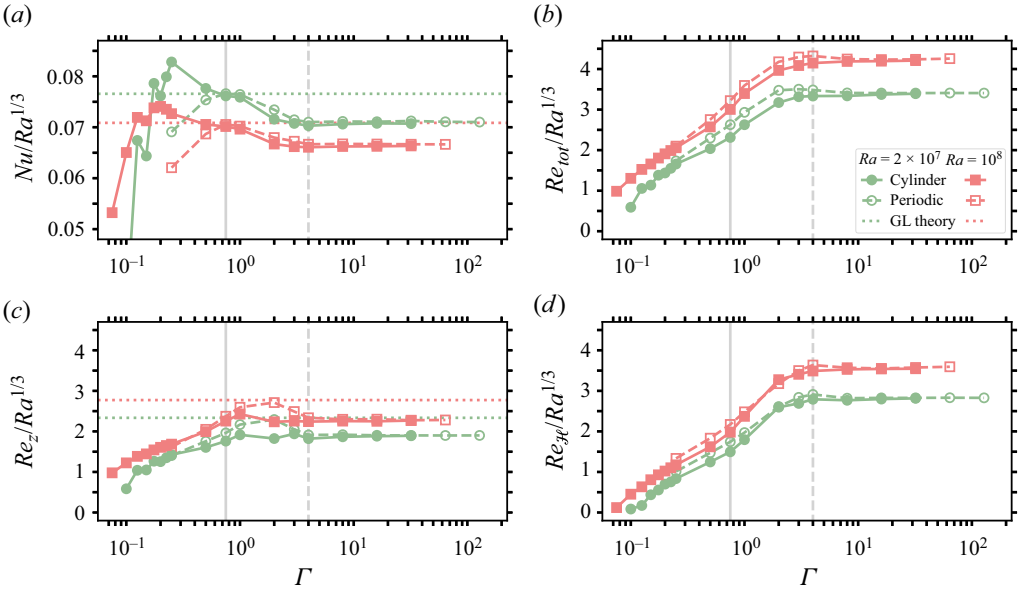

Figure 1. (*a*) Dimensionless heat transport *Nu* and (*b*) total, (*c*) vertical and (*d*) horizontal Reynolds numbers Re_{tot}, Re_z and $Re_{\mathcal{H}}$, respectively, as functions of Γ in a periodic and cylindrical domain for $Ra = 2 \times 10^7$ and 10^8 (periodic data from Stevens *et al.* 2018). The dotted lines show the prediction from the GL theory for a $\Gamma = 1$ cylinder (using the coefficients set in Stevens *et al.* 2013) for comparison. The vertical lines indicate $\Gamma = 0.75$ and 4. The jumps in *Nu* for small $\Gamma \sim 0.2$ are real, and reflect the transition between different flow states with different numbers of vertically staggered convection rolls; see the discussion of Zwirner & Shishkina (2018) and Zwirner, Tilgner & Shishkina (2020). They are not the focus of this paper.

vertical cross-section through the centre of the cell (figure 3), revealing many neighbouring convection rolls.

Figure 1 also shows the corresponding time- and volume-averaged vertical, horizontal and total *Re* as functions of Γ. The horizontal velocity increases continuously with Γ, before reaching its large-Γ limit, which is nearly identical in cylindrical and periodic domains (figure 1*d*). In contrast, the vertical velocity reaches a (not very pronounced) maximum at $\Gamma = 2$, while no maximum is observed in the data obtained from the cylindrical domain simulations (figure 1*c*). The total Re_{tot}, similarly to the horizontal $Re_{\mathcal{H}}$, increases continuously with Γ until the large-Γ limit is reached at $\Gamma \approx 4$. The predictions by the GL theory, which had been fitted to the *Re* data points from Qiu & Tong (2001) (cf. Grossmann & Lohse 2002; Stevens *et al.* 2013), are provided in figure 1(*c*). We emphasize that the equations of the GL theory allow for the transformation of the GL coefficients to different Reynolds number definitions or aspect ratios; see Grossmann & Lohse (2002) and Stevens *et al.* (2013). Comparing these results with the heat transport data in figure 1(*a*) demonstrates that changes in the overall flow strength are not necessarily reflected one-to-one in the heat transport.

4. Flow organization and statistics

This section focuses entirely on the data for $Ra = 10^8$. To gain more insight into the effect of the domain size on the flow characteristics, we analyse the variance profiles of the time and horizontally averaged temperature, horizontal and vertical velocity, respectively (figures 4 and 5). To enhance the statistical convergence, the statistics are averaged with

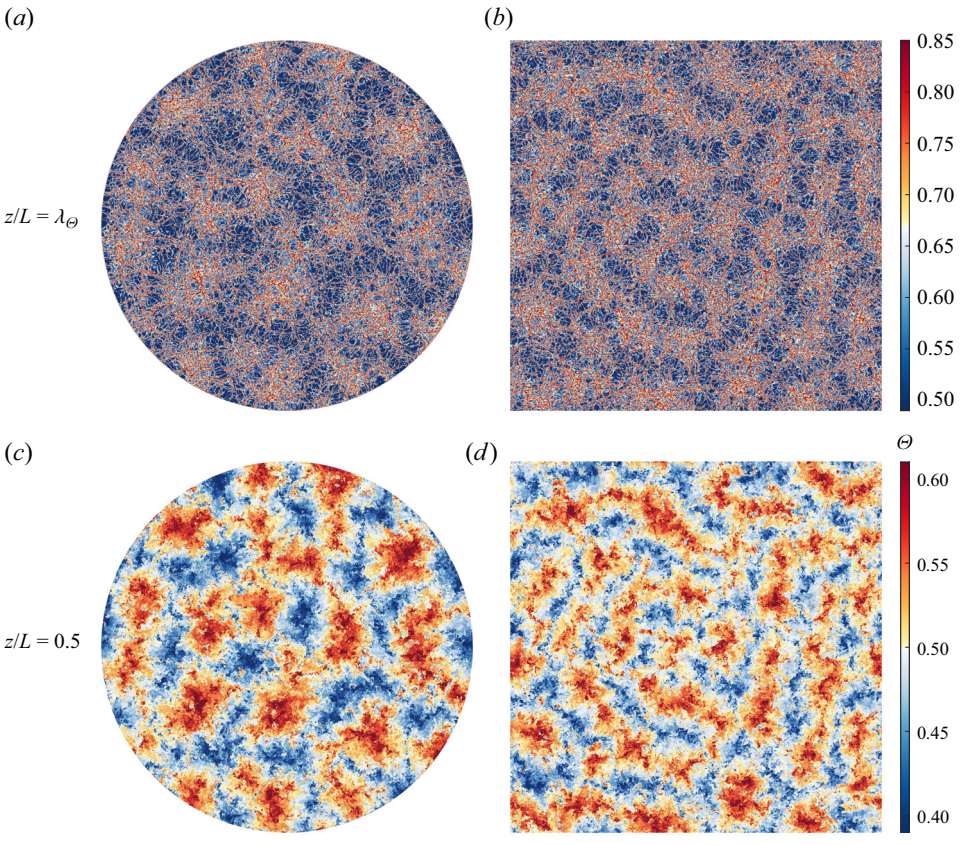

Figure 2. Snapshots of the temperature field Θ at (*a*,*b*) thermal BL height $z/L \approx 0.035$ and (*c*,*d*) mid-height $z/L = 0.5$, for simulations in (*a*,*c*) a cylindrical domain and (*b*,*d*) a periodic domain (data from Stevens *et al.* 2018), with $\Gamma = 32$ at $Ra = 10^8$. Panels for cylindrical and periodic domains are plotted on the same scale. The snapshots seem to suggest that large-scale flow structures are still slightly different in size in the periodic and cylindrical domains, even in the very large aspect ratio case $\Gamma = 32$ considered here. So large-scale structures do appear to be slightly affected by the sidewalls, but this is not affecting the overall heat transfer in the system.

Figure 3. Snapshots of the temperature field Θ in a vertical cross-section through the cell centre for simulations in a cylindrical domain for $\Gamma = 32$ at $Ra = 10^8$; colour map as in figure 2.

respect to the symmetry in the horizontal midplane. Figure 4 compares the vertical profiles obtained in cylindrical and periodic domains for $\Gamma \geq 1$. Towards large Γ, the variance profiles are nearly identical for periodic and cylindrical domains. Crucially, the variance profiles are converged at $\Gamma \approx 8$ in periodic domains, but only at $\Gamma \approx 16$ in cylindrical domains, while the integral Nu and Re already converge at $\Gamma \approx 4$ (figure 1).

4.1. *Temperature variance*

Figure 6(*a*) shows the azimuthally and time averaged temperature variance in the vertical radial plane. Additionally, we compare the radial profiles of the temperature variance for the various aspect ratios at a fixed vertical location ($z/L \approx 0.035$) just above the BL height as a function of r/R, with R the cylinder radius (figure 7*a*), and measured with

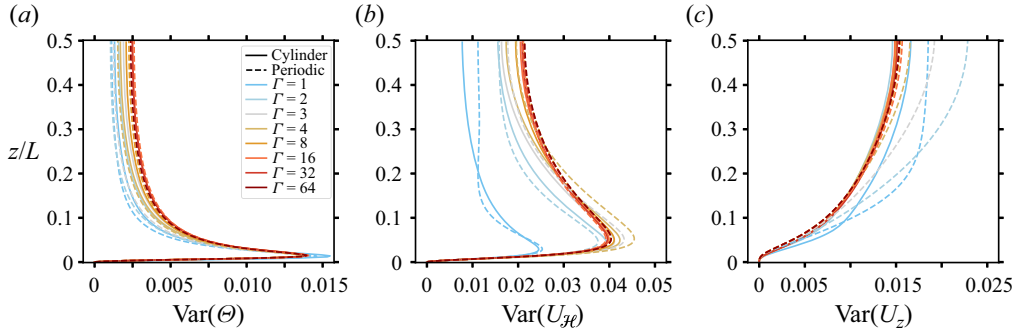

Figure 4. Comparison of the time and horizontally averaged variance of (*a*) temperature Θ, (*b*) horizontal velocity $U_{\mathcal{H}} = \sqrt{u_\varphi^2 + u_r^2}$, and (*c*) vertical velocity u_z, obtained in cylindrical (solid lines) and periodic (dashed lines; Stevens *et al.* 2018) domains for various aspect ratios Γ at $Ra = 10^8$.

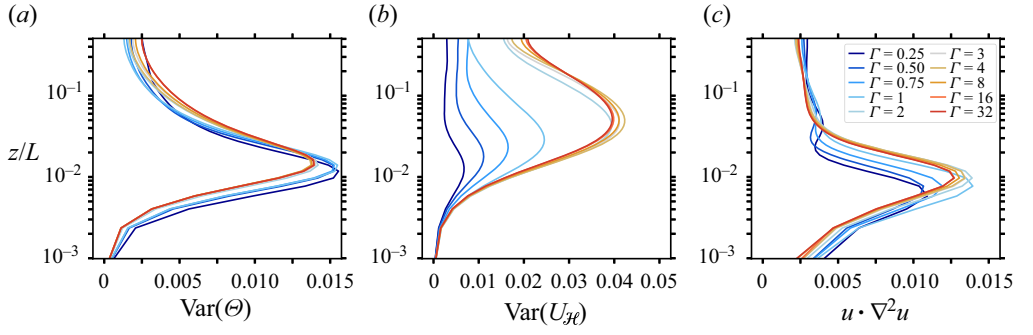

Figure 5. Vertical profile of the time and horizontally averaged variance of (*a*) temperature Θ, (*b*) horizontal velocity $U_{\mathcal{H}} = \sqrt{u_\varphi^2 + u_r^2}$, and (*c*) $\boldsymbol{u} \cdot \nabla^2 \boldsymbol{u}$ for various Γ at $Ra = 10^8$, plotted on a logarithmic scale to focus on the BL region. The vertical peak locations determine the BL thicknesses in figure 10.

respect to the sidewall (plotted as a function of $(R - r)/L$ in figure 7*b*). For large-Γ domains, the temperature variance is approximately uniform with radial position. Close to the sidewall, the temperature variance in smaller cells ($\Gamma \approx 1$) is similar to the values obtained in large-Γ cells. However, the temperature variance around the cylinder axis region is significantly lower in the smaller ($\Gamma \lesssim 1$) aspect ratio domains.

The radial profiles of the temperature variance (figures 7*a*,*b*) show some variation with radius r, even for the largest aspect ratio domains. The reason is that the time scale of the large-scale structures in RBC is very long, and therefore there remains an imprint of the thermal superstructures on the radially averaged profiles. This is demonstrated by the horizontal snapshots (figure 8) and time-averaged temperature fields in the horizontal midplane (figure 9), which reveal that these variations are due to the relatively limited movement of the thermal superstructures throughout the simulations. Related movies are provided in the supplementary material available at https://doi.org/10.1017/jfm.2024.996. These visualizations show that for $\Gamma \lesssim 1$, the LSC is found primarily in the region close to the sidewall, while the region around the cylinder axis shows fewer fluctuations. For $\Gamma \approx 4$, the LSC breaks up in multiple rolls such that fluctuations in the region around the cylinder axis increase. This agrees with previous experimental observations by Xia *et al.* (2008).

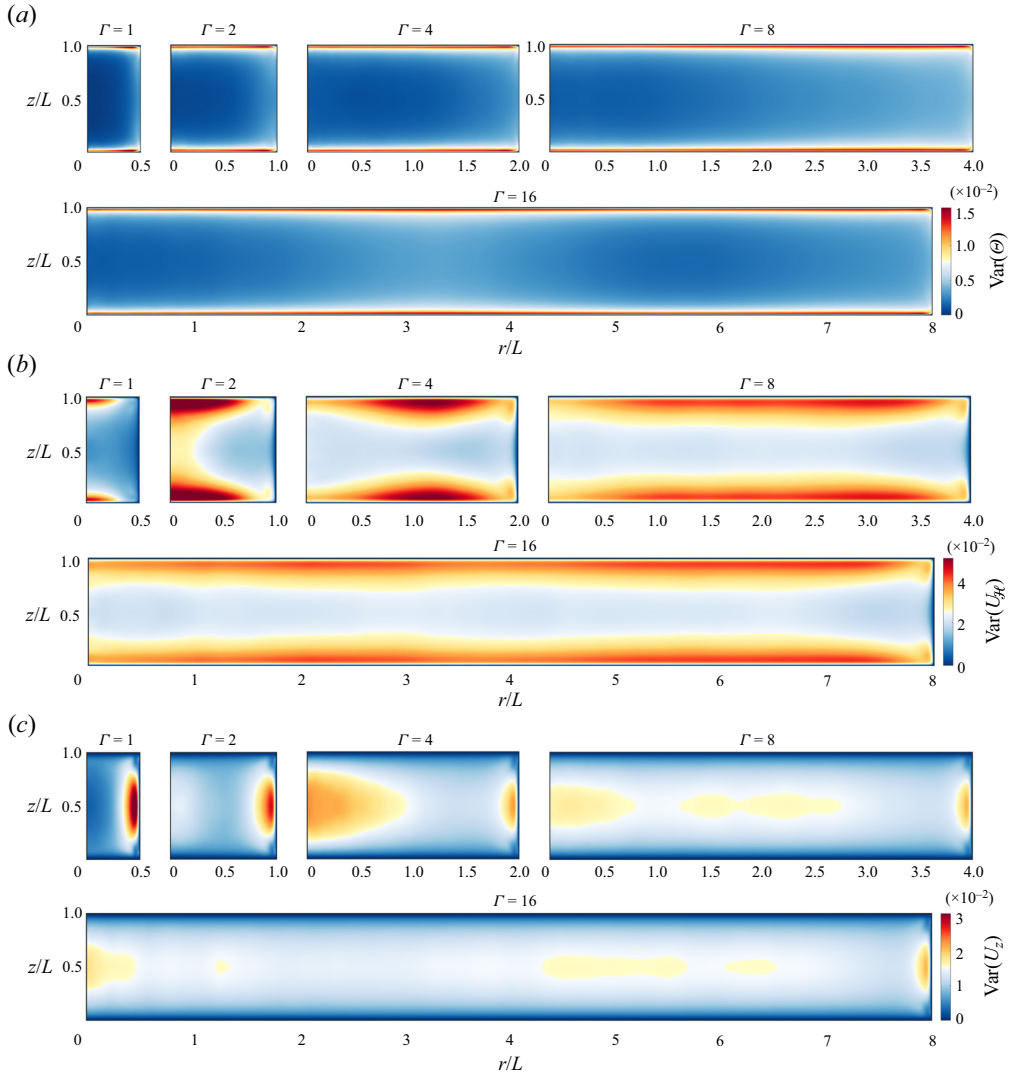

Figure 6. Azimuthally and time averaged variance of (a) temperature Θ, (b) horizontal velocity $U_{\mathcal{H}} = \sqrt{u_\varphi^2 + u_r^2}$, and ($c$) vertical velocity u_z in the vertical radial plane for cylindrical domains with aspect ratios $\Gamma = 1, 2, 4, 8, 16$ at $Ra = 10^8$.

4.2. *Horizontal velocity variance*

Figure 4(b) shows that close to the plate, the horizontal velocity variance peaks for $\Gamma = 4$. For larger Γ, the peak value then drops to the value obtained in the large-Γ limit. In contrast, in the bulk, the variance increases monotonically towards the large-Γ limit. This effect is most pronounced in the periodic domain, but is also evident in the cylindrical domain data (see figure 5b). This suggests that the monotonic increase for $\Gamma \lesssim 4$ and the subsequent saturation of the volume-averaged horizontal root mean square velocity $Re_{\mathcal{H}}$ (figure 1d) are determined mainly by the bulk. Figure 6(b) displays the horizontal velocity variance in the radial vertical plane, revealing an evident influence of large flow structures. For $\Gamma = 1$, the horizontal variance peaks in the region around the cylinder axis near the

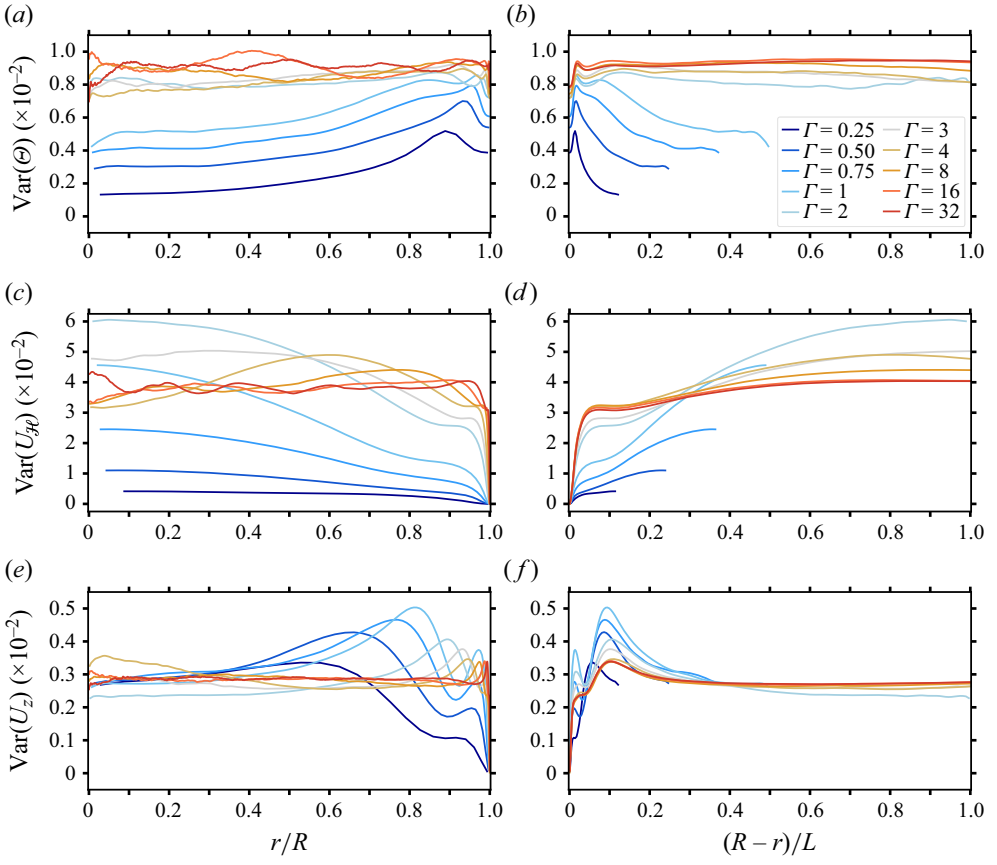

Figure 7. Radial profiles of azimuthally and time averaged variance of (*a*,*b*) the temperature Θ, (*c*,*d*) the horizontal velocity $U_{\mathcal{H}} = \sqrt{u_\varphi^2 + u_r^2}$, and (*e*,*f*) the vertical velocity u_z at $z/L \approx 0.035$ for $0.25 \leqslant \Gamma \leq 32$ and $Ra = 10^8$, (*a*,*c*,*e*) normalized by the outer radius R and (*b*,*d*,*f*) measured relative to the sidewall.

plate, where the LSC is most prominent. The horizontal velocity variance intensifies in a $\Gamma = 2$ cell before dropping to the large-Γ limit. For $\Gamma \gtrsim 8$, the horizontal variance becomes approximately constant throughout the domain. However, it is noteworthy that the imprint of the location of the thermal superstructures is more pronounced in the horizontal velocity variance than in the temperature variance. Remarkably, the radial horizontal velocity variance profile exhibits a pronounced structure when considered in the reference frame of the sidewall (figure 7*d*). This shows that thermal superstructures cannot form at the sidewall but require sufficient space to develop. This finding aligns with the observations of Weiss *et al.* (2010), who demonstrated that vertically aligned vortices in rotating RBC can form only at a certain distance from the sidewall.

4.3. *Vertical velocity variance*

The variance profiles of the time and horizontally averaged vertical velocity (figure 4*c*) show that in a periodic domain with $1 \leqslant \Gamma \leq 4$, the variance is higher than in the large-Γ limit. Further, the radial vertical representations in figure 6(*c*) reveal that for $\Gamma = 1$ and 2, the vertical velocity variance strongly peaks along the sidewall, while it decreases near

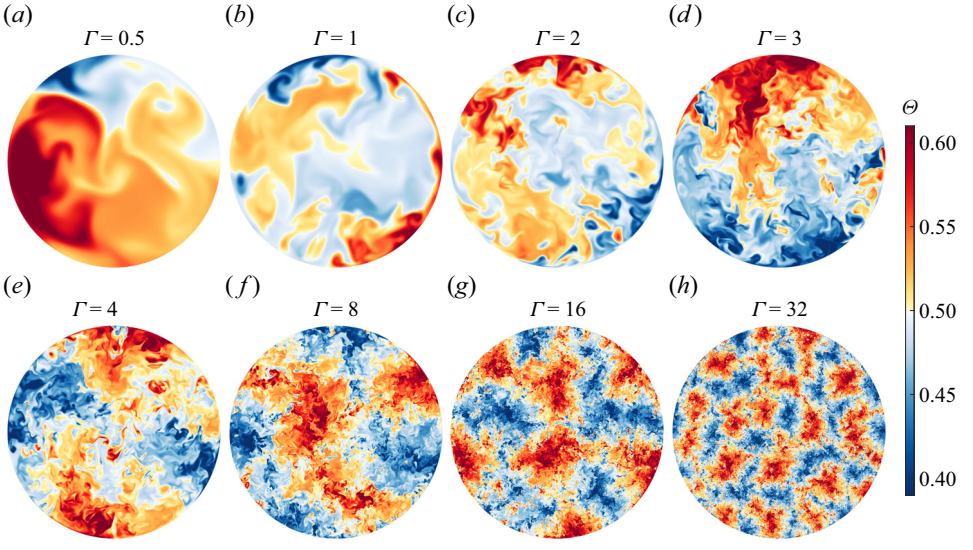

Figure 8. Snapshots of the temperature Θ at mid-height in cylindrical domains for different Γ at $Ra = 10^8$.

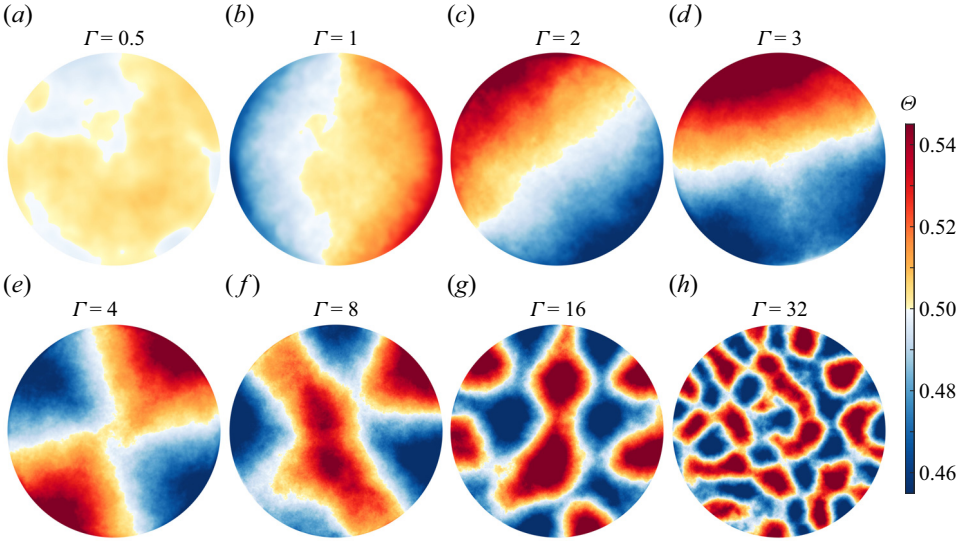

Figure 9. Time-averaged temperature $\langle\Theta\rangle_t$ at mid-height in cylindrical domains for different Γ at $Ra = 10^8$.

the central axis where the LSC is absent. With increasing aspect ratio, the vertical velocity variance becomes more uniform throughout the domain, with only a small peak remaining relatively close to the sidewall. Like the horizontal velocity variance, the radial profile in the reference frame of the sidewall reveals that the thermal superstructures require space to develop.

4.4. *Boundary layer thicknesses*

For completeness and to further demonstrate the effect of the domain aspect ratio, we determine the kinetic and thermal BL thicknesses (figure 10) using definitions commonly

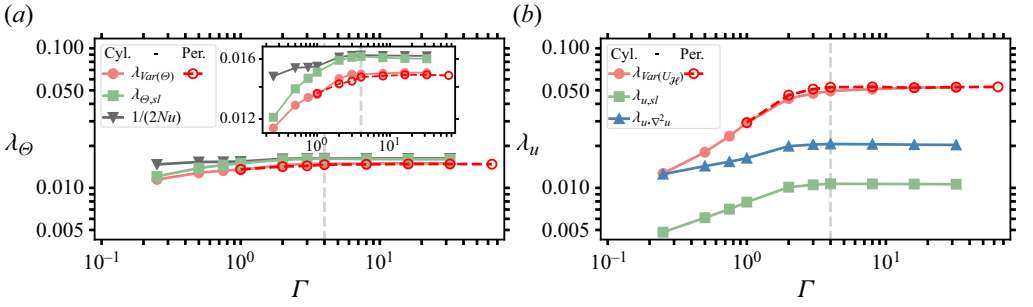

Figure 10. (*a*) Thermal and (*b*) kinetic/viscous BL thicknesses estimated from various definitions (see main text) for $Ra = 10^8$. The vertical dashed line indicates $\Gamma = 4$, beyond which integral quantities Nu and Re are converged (figure 1). For better comparison, (*a*) and (*b*) have the same scales not only on the horizontal Γ axis, but also on the vertical axis. The inset in (*a*) shows a zoom of the main figure in the λ_Θ range of interest.

employed in the literature (Ahlers *et al.* 2009). We present the kinetic BL thickness based on the peak position of the horizontal velocity variances (figure 4*b*), based on the slope method (Wagner, Shishkina & Wagner 2012), and based on twice the height of the peak position of $\boldsymbol{u} \cdot \nabla^2 \boldsymbol{u}$ (figure 5*c*); see Stevens, Clercx & Lohse (2010*a*) and Stevens *et al.* (2010*b*, 2011). For the thermal BL thickness, we report the values based on the variance peak (figure 4*a*) and the thermal BL thickness based on the slope method (Stevens *et al.* 2010*a*), and compare them with the classical $1/(2\,Nu)$ estimate. Figure 10 shows that the BL thicknesses obtained from these common definitions vary significantly with Γ. In particular, $\lambda_{Var(U_{\mathcal{H}})}$ increases by approximately a factor 5 with increasing Γ. This demonstrates that the three most common methods to estimate a kinetic BL thickness depict different BL heights of different quantities with possibly different physical meanings. We note that it has been found and analysed in many numerical Rayleigh–Bénard papers (Stevens *et al.* 2010*a*,*b*, 2011; Wagner *et al.* 2012; Hartmann *et al.* 2023) that different definitions of the BL thickness lead to different results, reflecting the different physics entering in the respective definitions.

We note that Berghout, Baars & Krug (2021) developed a conditional averaging technique with the LSC orientation to investigate the BL statistics more accurately. Subsequently, Blass *et al.* (2021) utilize this conditional averaging technique to extract LSC statistics, including the wall shear stress distribution, BL thicknesses, and the wind Reynolds number. In particular, they show that various properties of the LSC obtained here, such as the wall shear stress distribution, the BL thicknesses and the wind Re, do not differ significantly in large and small (i.e. $\Gamma = 1$) aspect ratio domains. This explains why changes in the large-scale flow organization are not necessarily reflected in the heat transfer.

5. Conclusions and outlook

In conclusion, we investigated the heat transfer in cylindrical convection cells and periodic domains using DNS of turbulent RBC, spanning an unprecedentedly wide range of aspect ratios $0.075 \leqslant \Gamma \leqslant 32$. In both cases, with increasing aspect ratio, the heat transfer first increases, then reaches a maximum (which is more pronounced for the cylindrical case due to the confinement effect), and then slightly goes down again before it finally saturates at the large aspect ratio limit, which already is achieved at $\Gamma \approx 4$. Already for $\Gamma \gtrsim 0.75$, the heat transfers in both laterally periodic and cylindrical domains become identical. For the

total Re, the finite-size effects also disappear for $\Gamma \gtrsim 4$ in both periodic and cylindrical domains. This indicates that changes in the large-scale flow structures do not necessarily impact the heat transfer, which is primarily governed by the boundary layer (BL) dynamics (Ahlers *et al.* 2009; Blass *et al.* 2021).

While for integral quantities finite-size effects disappear for $\Gamma \gtrsim 4$, they vanish only at $\Gamma \approx 16$ for the variances. In smaller cylindrical cells, the cylindrical geometry strongly influences the distribution of the temperature and velocity fluctuations in the radial vertical projection. Both horizontal and vertical velocity profiles reveal that thermal superstructures require sufficient space for their development, as they cannot form near the sidewall. Finally, the one-to-one comparison between RBC in periodic and confined cylindrical domains reveals that integral flow properties and vertical variance profiles indicating flow characteristics become identical in the large-Γ limit when the domain is larger than the typical size of the thermal superstructures.

Overall, our analysis reveals that for $\Gamma \gtrsim 0.75$, the heat transfer – governed primarily by BL dynamics – is identical in laterally periodic and cylindrical domains. This indicates that the effects of confinement on the heat transfer are limited. The large aspect ratio limit for heat transfer is already attained at $\Gamma \approx 4$. In contrast, differences in the organization of the large-scale flow, as manifested in the variance profiles, persist up to $\Gamma \approx 16$, attributed to the inability of turbulent superstructures to form near the sidewalls.

We now come to an outlook towards much larger Ra. What follows from our study for the choice of an 'optimal' configuration or geometry to achieve the ultimate regime of RBC in DNS? Here, 'optimal' is meant in the sense of having the smallest possible computational domain, but yet to achieve the ultimate regime (i.e. to maximize the range between the maximal accessible Ra and the critical Ra for the onset of convection), and by 'ultimate' regime we mean the regime in which Nu scales more steeply with Ra than with $Nu \sim Ra^{1/3}$, due to the transition of a laminar type BL to a turbulent type BL with enhanced heat transfer properties (Kraichnan 1962; Lohse & Shishkina 2023). For a cylindrical cell, Shishkina (2021) had already shown that such an optimal choice is $\Gamma \approx 0.5$, and this present study demonstrates that for such a choice, the heat transfer is nearly the same as in the $\Gamma \to \infty$ case. For the horizontally periodic case, which generally is computationally cheaper, our study suggests that $\Gamma \approx 0.75$ is the best choice (i.e. computationally cheapest) to achieve the ultimate regime, as that case requires the least laterally extended grid without much affecting the heat transfer. We note, however, that given that the transition to the ultimate regime is of non-normal nonlinear nature (Roche 2020; Lohse & Shishkina 2023), a restriction to the aspect ratios of the periodic box may affect how much disturbances in the BL can grow and thus how they can trigger the transition to the ultimate regime.

Supplementary material. Supplementary movies are available at https://doi.org/10.1017/jfm.2024.996.

Funding. We thank O. Shishkina for helpful discussions and comments. This work is supported by the European Research Council (ERC) starting grant no. 804283 UltimateRB and the ERC advanced grant no. 101094492 MultiMelt. The authors gratefully acknowledge the Gauss Centre for Supercomputing e.V. (www.gauss-centre.eu) for funding this project by providing computing time on the GCS Supercomputer SuperMUC-NG at Leibniz Supercomputing Centre (www.lrz.de).

Declaration of interests. The authors report no conflict of interest.

Author ORCIDs.
Richard J.A.M. Stevens https://orcid.org/0000-0001-6976-5704;
Robert Hartmann https://orcid.org/0000-0002-4860-0449;

Ra	Γ	$N_\vartheta \times N_r \times N_z$	Nu	Re_ϑ	Re_r	Re_z	Re_{tot}	δt_{avg}
2×10^7	0.100	$64 \times 16 \times 128$	9.03 (9.03)	17.37	15.25	158.68	160.35	10 000
2×10^7	0.125	$64 \times 16 \times 128$	18.30 (18.30)	34.21	32.11	282.64	286.51	10 000
2×10^7	0.150	$64 \times 16 \times 128$	17.47 (17.47)	91.15	75.94	284.87	308.59	10 000
2×10^7	0.175	$64 \times 16 \times 128$	21.34 (21.34)	119.22	92.27	343.37	375.00	10 000
2×10^7	0.200	$64 \times 16 \times 128$	20.67 (20.67)	152.12	113.87	340.47	389.90	10 000
2×10^7	0.225	$64 \times 16 \times 128$	21.69 (21.80)	159.70	128.27	366.54	421.01	10 000
2×10^7	0.25	$96 \times 16 \times 128$	22.48 (22.29)	175.27	144.19	386.94	449.86	10 000
2×10^7	0.50	$192 \times 32 \times 128$	21.07 (21.08)	248.37	229.73	435.71	552.83	10 000
2×10^7	0.75	$256 \times 48 \times 128$	20.67 (20.69)	295.02	279.17	477.78	627.80	10 000
2×10^7	1.0	$384 \times 64 \times 128$	20.60 (20.59)	359.61	328.87	519.89	713.00	10 000
2×10^7	2.0	$768 \times 128 \times 128$	19.43 (19.42)	535.25	458.57	495.16	861.37	640
2×10^7	3.0	$1152 \times 192 \times 128$	19.21 (19.19)	604.97	409.00	526.66	900.36	640
2×10^7	4.0	$1536 \times 256 \times 128$	19.08 (19.08)	610.57	449.14	494.28	904.90	639
2×10^7	8.0	$3072 \times 512 \times 128$	19.17 (19.18)	537.09	525.17	506.69	906.10	648
2×10^7	16.0	$6144 \times 1024 \times 128$	19.21 (19.21)	560.78	511.98	510.87	915.20	640
2×10^7	32.0	$12\,288 \times 2048 \times 128$	19.19 (19.19)	555.38	524.83	513.72	920.76	280
1×10^8	0.075	$144 \times 24 \times 192$	24.71 (24.71)	41.30	38.26	453.96	457.44	10 000
1×10^8	0.100	$144 \times 24 \times 192$	30.19 (30.19)	165.71	128.22	568.02	605.43	10 000
1×10^8	0.125	$144 \times 24 \times 192$	33.39 (32.91)	233.80	178.13	642.79	707.80	10 000
1×10^8	0.150	$144 \times 24 \times 192$	33.08 (33.16)	294.36	232.30	670.89	768.57	10 000
1×10^8	0.175	$144 \times 24 \times 192$	34.26 (34.24)	333.47	273.28	716.49	836.21	10 000
1×10^8	0.200	$144 \times 24 \times 192$	34.39 (34.40)	362.20	306.38	746.00	884.07	10 000
1×10^8	0.225	$144 \times 24 \times 192$	34.13 (34.16)	387.38	334.66	766.45	921.69	10 000
1×10^8	0.25	$144 \times 24 \times 192$	33.73 (33.66)	410.30	359.23	782.49	953.77	2000
1×10^8	0.50	$288 \times 48 \times 192$	32.75 (32.74)	552.03	510.68	925.73	1192.69	2000
1×10^8	0.75	$384 \times 72 \times 192$	32.56 (32.61)	678.17	620.52	1046.60	1392.96	2000
1×10^8	1.0	$576 \times 96 \times 192$	32.32 (32.23)	822.22	731.85	1126.69	1575.14	1000
1×10^8	2.0	$1152 \times 192 \times 192$	30.96 (30.88)	1154.20	989.72	1038.27	1841.12	380
1×10^8	3.0	$1728 \times 288 \times 192$	30.72 (30.72)	1226.57	998.97	1046.54	1896.74	400
1×10^8	4.0	$2304 \times 384 \times 192$	30.67 (30.62)	1283.40	988.28	1040.48	1925.20	380
1×10^8	8.0	$4608 \times 768 \times 192$	30.74 (30.77)	1228.34	1084.00	1046.23	1943.83	400
1×10^8	16.0	$9216 \times 1536 \times 192$	30.75 (30.75)	1209.08	1112.94	1044.11	1946.96	379
1×10^8	32.0	$18\,432 \times 3072 \times 192$	30.79 (30.79)	1179.21	1148.06	1052.47	1953.53	396

Table 1. The first two columns indicate Ra and Γ of the Rayleigh–Bénard flow simulations in cylindrical cells. The next columns indicate the resolution used in the azimuthal, radial and axial directions ($N_\vartheta \times N_r \times N_z$), Nu averaged over the full (and second half) of the time interval δt_{avg}, the time- and volume-averaged Re of the different velocity components, the total Re_{tot}, and the averaging interval δt_{avg} in free-fall time units L/U_{ff}. Note that the DNS of Bailon-Cuba *et al.* (2010) have considerable less spatial resolution for the large Γ cases. For $Ra = 10^8$, a one-to-one comparison with our DNS is provided in the Appendix.

Roberto Verzicco https://orcid.org/0000-0002-2690-9998;
Detlef Lohse https://orcid.org/0000-0003-4138-2255.

Appendix. Comparison to the data of Bailon-Cuba *et al.* (2010)

Following the suggestion of a referee, we include a detailed comparison of our present data with those of Bailon-Cuba *et al.* (2010); see table 2 for all available data, and figure 11 for the case $Ra = 10^8$. As can be seen, for larger $\Gamma > 2.5$, the Nusselt number Nu in the data of Bailon-Cuba *et al.* (2010) goes up considerably, which is a consequence of the increasingly insufficient grid resolution for the increasing Γ. It is not a physical effect.

		This study			Bailon-Cuba *et al.* (2010)		
Ra	Γ	$N_\vartheta \times N_r \times N_z$	Nu	δt_{avg}	$N_\vartheta \times N_r \times N_z$	Nu	δt_{avg}
1×10^8	0.075	$129 \times 24 \times 192$	24.71 (24.71)	10 000	—	—	—
1×10^8	0.100	$129 \times 24 \times 192$	30.19 (30.19)	10 000	—	—	—
1×10^8	0.125	$129 \times 24 \times 192$	33.39 (32.91)	10 000	—	—	—
1×10^8	0.150	$129 \times 24 \times 192$	33.08 (33.16)	10 000	—	—	—
1×10^8	0.175	$129 \times 24 \times 192$	34.26 (34.24)	10 000	—	—	—
1×10^8	0.200	$129 \times 24 \times 192$	34.39 (34.40)	10 000	—	—	—
1×10^8	0.225	$129 \times 24 \times 192$	34.13 (34.16)	10 000	—	—	—
1×10^8	0.25	$144 \times 24 \times 192$	33.73 (33.66)	2000	—	—	—
1×10^8	0.50	$288 \times 48 \times 192$	32.75 (32.74)	2000	$151 \times 101 \times 256$	32.06 ± 0.24	300
1×10^8	0.75	$384 \times 72 \times 192$	32.56 (32.61)	2000	—	—	—
1×10^8	1.0	$576 \times 96 \times 192$	32.32 (32.23)	1000	$271 \times 151 \times 256$	32.21 ± 0.32	150
1×10^8	1.25	—	—	—	$271 \times 151 \times 256$	31.77 ± 0.15	150
1×10^8	1.5	—	—	—	$321 \times 161 \times 256$	31.39 ± 0.11	150
1×10^8	1.75	—	—	—	$321 \times 161 \times 256$	31.57 ± 0.10	249
1×10^8	2.0	$1152 \times 192 \times 192$	30.96 (30.88)	380	$361 \times 181 \times 256$	31.25 ± 0.31	145
1×10^8	2.25	—	—	—	$401 \times 201 \times 256$	31.25 ± 0.21	143
1×10^8	2.5	—	—	—	$401 \times 201 \times 256$	31.87 ± 0.18	146
1×10^8	2.75	—	—	—	$401 \times 201 \times 256$	32.34 ± 0.08	145
1×10^8	3.0	$1728 \times 288 \times 192$	30.72 (30.72)	400	$451 \times 225 \times 256$	32.29 ± 0.12	141
1×10^8	4.0	$2304 \times 384 \times 192$	30.67 (30.62)	380	$541 \times 257 \times 256$	33.20 ± 0.08	132
1×10^8	8.0	$4608 \times 768 \times 192$	30.74 (30.77)	400	$801 \times 451 \times 256$	34.78 ± 0.13	81
1×10^8	16.0	$9216 \times 1536 \times 192$	30.75 (30.75)	379	—	—	—
1×10^8	32.0	$18\,432 \times 3072 \times 192$	30.79 (30.79)	396	—	—	—

Table 2. The first two columns indicate Ra and Γ of the simulation. The next columns indicate the resolution used in the azimuthal, radial and axial directions ($N_\vartheta \times N_r \times N_z$), Nu averaged over the full (and second half) of the time interval δt_{avg}, and the averaging interval δt_{avg} in free-fall time units L/U_{ff} for the cases in this study, followed by resolution in the azimuthal, radial and axial directions ($N_\vartheta \times N_r \times N_z$), Nu, and the averaging interval δt_{avg} in free-fall time units as stated in Bailon-Cuba *et al.* (2010).

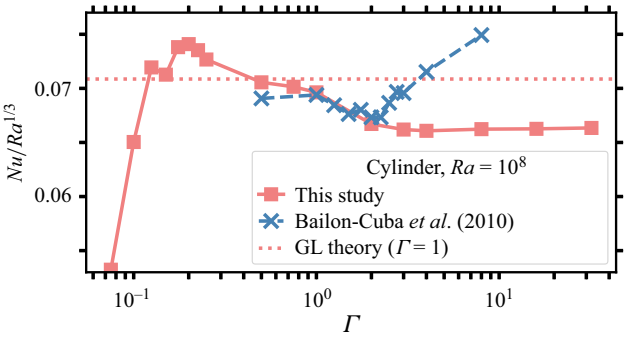

Figure 11. Plots of $Nu/Ra^{1/3}$ versus Γ for $Ra = 10^8$ for the cylindrical cell: Comparison of data of this paper (red boxes) and of the data of Bailon-Cuba *et al.* (2010) (blue crosses), which seem to be under-resolved for large Γ; see table 2. The increase of Nu in the latter for larger $\Gamma > 2.5$ is due to the lack of sufficient grid resolution for those large-Γ cases and presumably also due to lack of sufficient statistical averaging. The dotted line shows the prediction from the GL theory for a $\Gamma = 1$ cylinder (using the coefficients set in Stevens *et al.* 2013) for comparison.

References

Ahlers, G., *et al.* 2022 Aspect ratio dependence of heat transfer and flow dynamics in a cylindrical Rayleigh–Bénard cell. *Phys. Rev. Lett.* **128**, 084501.

Ahlers, G., Grossmann, S. & Lohse, D. 2009 Heat transfer and large scale dynamics in turbulent Rayleigh–Bénard convection. *Rev. Mod. Phys.* **81**, 503–537.

Bailon-Cuba, J., Emran, M.S. & Schumacher, J. 2010 Aspect ratio dependence of heat transfer and large-scale flow in turbulent convection. *J. Fluid Mech.* **655**, 152–173.

Berghout, P., Baars, W.J. & Krug, D.J. 2021 The large-scale footprint in small-scale Rayleigh–Bénard turbulence. *J. Fluid Mech.* **911**, A62.

Blass, A., Verzicco, R., Lohse, D., Stevens, R.J.A.M. & Krug, D.J. 2021 Flow organization in laterally unconfined Rayleigh–Bénard turbulence. *J. Fluid Mech.* **906**, A26.

Bodenschatz, E., Pesch, W. & Ahlers, G. 2000 Recent developments in Rayleigh–Bénard convection. *Annu. Rev. Fluid Mech.* **32**, 709–778.

Charlson, G.S. & Sani, R.L. 1970 Thermoconvective instability in a bounded cylindrical fluid layer. *Intl J. Heat Mass Transfer* **13** (9), 1479–1496.

Chavanne, X., Chilla, F., Castaing, B., Hebral, B., Chabaud, B. & Chaussy, J. 1997 Observation of the ultimate regime in Rayleigh–Bénard convection. *Phys. Rev. Lett.* **79**, 3648–3651.

Chilla, F. & Schumacher, J. 2012 New perspectives in turbulent Rayleigh–Bénard convection. *Eur. Phys. J.* E **35**, 58.

Chong, K.L., Huang, S.-D., Kaczorowski, M. & Xia, K.-Q. 2015 Condensation of coherent structures in turbulent flows. *Phys. Rev. Lett.* **115**, 264503.

Chong, K.L., Yang, Y., Huang, S.-D., Zhong, J.-Q., Stevens, R.J.A.M., Verzicco, R., Lohse, D. & Xia, K.-Q. 2017 Confined Rayleigh–Bénard, rotating Rayleigh–Bénard, and double diffusive convection: a unifying view on turbulent transport enhancement through coherent structure manipulation. *Phys. Rev. Lett.* **119** (6), 064501.

Emran, M.S. & Schumacher, J. 2015 Large-scale mean patterns in turbulent convection. *J. Fluid Mech.* **776**, 96–108.

Fitzjarrald, D.E. 1976 An experimental study of turbulent convection in air. *J. Fluid Mech.* **73** (4), 693–719.

Grossmann, S. & Lohse, D. 2000 Scaling in thermal convection: a unifying view. *J. Fluid Mech.* **407**, 27–56.

Grossmann, S. & Lohse, D. 2001 Thermal convection for large Prandtl number. *Phys. Rev. Lett.* **86**, 3316–3319.

Grossmann, S. & Lohse, D. 2002 Prandtl and Rayleigh number dependence of the Reynolds number in turbulent thermal convection. *Phys. Rev.* E **66**, 016305.

Grossmann, S. & Lohse, D. 2004 Fluctuations in turbulent Rayleigh–Bénard convection: the role of plumes. *Phys. Fluids* **16**, 4462–4472.

Grossmann, S. & Lohse, D. 2011 Multiple scaling in the ultimate regime of thermal convection. *Phys. Fluids* **23**, 045108.

von Hardenberg, J., Parodi, A., Passoni, G., Provenzale, A. & Spiegel, E.A. 2008 Large-scale patterns in Rayleigh–Bénard convection. *Phys. Lett.* A **372**, 2223–2229.

Hartlep, T., Tilgner, A. & Busse, F.H. 2003 Large scale structures in Rayleigh–Bénard convection at high Rayleigh numbers. *Phys. Rev. Lett.* **91**, 064501.

Hartlep, T., Tilgner, A. & Busse, F.H. 2005 Transition to turbulent convection in a fluid layer heated from below at moderate aspect ratio. *J. Fluid Mech.* **544**, 309–322.

Hartmann, R., Chong, K.L., Stevens, R.J.A.M., Verzicco, R. & Lohse, D. 2021 Heat transport enhancement in confined Rayleigh–Bénard convection feels the shape of the container. *Europhys. Lett.* **135** (2), 24004.

Hartmann, R., Verzicco, R., Kranenbarg, L.K., Lohse, D. & Stevens, R.J.A.M. 2022 Multiple heat transport maxima in confined-rotating Rayleigh–Bénard convection. *J. Fluid Mech.* **939**, A1.

Hartmann, R., Yerragolam, G.S., Verzicco, R., Lohse, D. & Stevens, R.J.A.M. 2023 Optimal heat transport in rotating Rayleigh–Bénard convection at large Rayleigh numbers. *Phys. Rev. Fluids* **8**, 083501.

He, X., Funfschilling, D., Nobach, H., Bodenschatz, E. & Ahlers, G. 2012 Transition to the ultimate state of turbulent Rayleigh–Bénard convection. *Phys. Rev. Lett.* **108**, 024502.

Hogg, J. & Ahlers, G. 2013 Reynolds-number measurements for low-Prandtl-number turbulent convection of large-aspect-ratio samples. *J. Fluid Mech.* **725**, 664–680.

Huang, S.D., Kaczorowski, M., Ni, R. & Xia, K.-Q. 2013 Confinement-induced heat-transport enhancement in turbulent thermal convection. *Phys. Rev. Lett.* **111** (10), 104501.

KOOIJ, G.L., BOTCHEV, M.A., FREDERIX, E.M.A., GEURTS, B.J., HORN, S., LOHSE, D., VAN DER POEL, E.P., SHISHKINA, O., STEVENS, R.J.A.M. & VERZICCO, R. 2018 Comparison of computational codes for direct numerical simulations of turbulent Rayleigh–Bénard convection. *Comput. Fluids* **166**, 1–8.

KRAICHNAN, R.H. 1962 Turbulent thermal convection at arbitrary Prandtl number. *Phys. Fluids* **5**, 1374–1389.

KRUG, D.J., LOHSE, D. & STEVENS, R.J.A.M. 2020 Coherence of temperature and velocity superstructures in turbulent Rayleigh–Bénard flow. *J. Fluid Mech.* **887**, A2.

LOHSE, D. & SHISHKINA, O. 2023 Ultimate turbulent thermal convection. *Phys. Today* **76** (11), 26–32.

LOHSE, D. & XIA, K.-Q. 2010 Small-scale properties of turbulent Rayleigh–Bénard convection. *Annu. Rev. Fluid Mech.* **42**, 335–364.

PANDEY, A., SCHEEL, J.D. & SCHUMACHER, J. 2018 Turbulent superstructures in Rayleigh–Bénard convection. *Nat. Commun.* **9** (1), 2118.

PARODI, A., VON HARDENBERG, J., PASSONI, G., PROVENZALE, A. & SPIEGEL, E.A. 2004 Clustering of plumes in turbulent convection. *Phys. Rev. Lett.* **92**, 194503.

DU PUITS, R., RESAGK, C. & THESS, A. 2007 Breakdown of wind in turbulent thermal convection. *Phys. Rev.* E **75**, 016302.

DU PUITS, R., RESAGK, C. & THESS, A. 2013 Thermal boundary layers in turbulent Rayleigh–Bénard convection at aspect ratios between 1 and 9. *New J. Phys.* **15**, 013040.

QIU, X.L. & TONG, P. 2001 Large scale velocity structures in turbulent thermal convection. *Phys. Rev.* E **64**, 036304.

REN, L., TAO, X., XIA, K.-Q. & XIE, Y.-C. 2024 Transition to fully developed turbulence in liquid-metal convection facilitated by spatial confinement. *J. Fluid Mech.* **981**, R2.

ROCHE, P.E. 2020 The ultimate state of convection: a unifying picture of very high Rayleigh numbers experiments. *New J. Phys.* **22**, 073056.

ROCHE, P.E., GAUTHIER, G., KAISER, R. & SALORT, J. 2010 On the triggering of the ultimate regime of convection. *New J. Phys.* **12**, 085014.

SAKIEVICH, P.J., PEET, Y.T. & ADRIAN, R.J. 2016 Large-scale thermal motions of turbulent Rayleigh–Bénard convection in a wide aspect-ratio cylindrical domain. *Intl J. Heat Mass Transfer* **61**, 183–196.

SHISHKINA, O. 2021 Rayleigh–Bénard convection: the container shape matters. *Phys. Rev. Fluids* **6**, 090502.

SHISHKINA, O., STEVENS, R.J.A.M., GROSSMANN, S. & LOHSE, D. 2010 Boundary layer structure in turbulent thermal convection and its consequences for the required numerical resolution. *New J. Phys.* **12**, 075022.

SHISHKINA, O. & WAGNER, C. 2005 A fourth order accurate finite volume scheme for numerical simulations of turbulent Rayleigh–Bénard convection in cylindrical containers. *C. R. Méc.* **333**, 17–28.

SHISHKINA, O. & WAGNER, C. 2006 Analysis of thermal dissipation rates in turbulent Rayleigh–Bénard convection. *J. Fluid Mech.* **546**, 51–60.

SPIEGEL, E.A. 1972 Convection in stars II. Special effects. *Annu. Rev. Astron. Astrophys.* **10**, 261–304.

STEVENS, R.J.A.M., BLASS, A., ZHU, X., VERZICCO, R. & LOHSE, D. 2018 Turbulent thermal superstructures in Rayleigh–Bénard convection. *Phys. Rev. Fluids* **3**, 041501(R).

STEVENS, R.J.A.M., CLERCX, H.J.H. & LOHSE, D. 2010*a* Boundary layers in rotating weakly turbulent Rayleigh–Bénard convection. *Phys. Fluids* **22**, 085103.

STEVENS, R.J.A.M., LOHSE, D. & VERZICCO, R. 2011 Prandtl and Rayleigh number dependence of heat transport in high Rayleigh number thermal convection. *J. Fluid Mech.* **688**, 31–43.

STEVENS, R.J.A.M., VAN DER POEL, E.P., GROSSMANN, S. & LOHSE, D. 2013 The unifying theory of scaling in thermal convection: the updated prefactors. *J. Fluid Mech.* **730**, 295–308.

STEVENS, R.J.A.M., VERZICCO, R. & LOHSE, D. 2010*b* Radial boundary layer structure and Nusselt number in Rayleigh–Bénard convection. *J. Fluid Mech.* **643**, 495–507.

SUN, C., REN, L.-Y., SONG, H. & XIA, K.-Q. 2005 Heat transport by turbulent Rayleigh–Bénard convection in 1 m diameter cylindrical cells of widely varying aspect ratio. *J. Fluid Mech.* **542**, 165–174.

VERZICCO, R. & CAMUSSI, R. 1997 Transitional regimes of low-Prandtl thermal convection in a cylindrical cell. *Phys. Fluids* **9**, 1287–1295.

VERZICCO, R. & ORLANDI, P. 1996 A finite-difference scheme for three-dimensional incompressible flow in cylindrical coordinates. *J. Comput. Phys.* **123**, 402–413.

WAGNER, S., SHISHKINA, O. & WAGNER, C. 2012 Boundary layers and wind in cylindrical Rayleigh–Bénard cells. *J. Fluid Mech.* **697**, 336–366.

WEISS, S., STEVENS, R.J.A.M., ZHONG, J.-Q., CLERCX, H.J.H., LOHSE, D. & AHLERS, G. 2010 Finite-size effects lead to supercritical bifurcations in turbulent rotating Rayleigh–Bénard convection. *Phys. Rev. Lett.* **105**, 224501.

XIA, K.-Q. 2013 Current trends and future directions in turbulent thermal convection. *Theor. Appl. Mech. Lett.* **3**, 052001.

XIA, K.-Q., HUANG, S.-D., XIE, Y.-C. & ZHANG, L. 2023 Tuning heat transport via coherent structure manipulation: recent advances in thermal turbulence. *Natl Sci. Rev.* **10** (6), nwad012.

XIA, K.-Q., SUN, C. & CHEUNG, Y.-H. 2008 Large scale velocity structures in turbulent thermal convection with widely varying aspect ratio. In *14th International Symposium on Applications of Laser Techniques to Fluid Mechanics*, pp. 1–4.

ZHANG, L. & XIA, K.-Q. 2023 Heat transfer in a quasi-one-dimensional Rayleigh–Bénard convection cell. *J. Fluid Mech.* **973**, R5.

ZHOU, Q., LIU, B.-F., LI, C.-M. & ZHONG, B.-C. 2012 Aspect ratio dependence of heat transport by turbulent Rayleigh–Bénard convection in rectangular cells. *J. Fluid Mech.* **710**, 260–276.

ZWIRNER, L. & SHISHKINA, O. 2018 Confined inclined thermal convection in low-Prandtl-number fluids. *J. Fluid Mech.* **850**, 984–1008.

ZWIRNER, L., TILGNER, A. & SHISHKINA, O. 2020 Elliptical instability and multi-roll flow modes of the large-scale circulation in confined turbulent Rayleigh–Bénard convection. *Phys. Rev. Lett.* **125** (5), 054502.